

Droplet Size Determination on a Rotary Atomizer Wheel with Time-Shift Technique in Comparison to Analytical Theory

Maximilian Kuhnhenn^{*1}, Aaron Oberthür², Ilia V. Roisman¹, Tórstein V. Joensen³, Cameron Tropea¹

¹Institute for Fluid Mechanics and Aerodynamics, Technische Universität Darmstadt, Darmstadt, Germany

²AOM-Systems GmbH, Griesheim, Germany

³GEA Process Engineering A/S, Soeborg, Denmark

*Corresponding author: Kuhnhenn@sla.tu-darmstadt.de

Abstract

Rotary atomizers are used in spray drying applications. Spray drying is a method of producing a dry powder from a fluid solution or slurry. The feedstock is atomized into droplets that are then dried rapidly into particles with a hot gas. Spray drying is widely used in the chemical and food industry and is the preferred method of drying of many materials such as dairy products, foods, pharmaceuticals, polymers and more. For the design of spray drying processes the droplet size distribution has to be known, to be able to predict the resultant powder size distribution. Based on initial assumptions regarding the flow inside the wheel, the behaviour of the feed within the inserts (radial opening of the wheel) is described with analytical equations and compared to numerical and experimental investigations. The liquid accumulates on the trailing edge of the insert and therefore the film thickness on the exit of the inserts is used to compare all approaches. A time-shift measurement technique is used to analyse droplet size and velocities of the resulting spray. In addition it allows to investigate the relationship between the jet thickness and the resulting sauter mean diameter D_{32} of the droplets.

Introduction

The droplet size distribution in spray drying processes [1] or flue gas cleaning [2] with rotary atomizer wheels, has a significant impact on the outcome of the process, e.g. the properties of the dried powder. The intended use of the dried powder determines the desired size distribution of the powder particles, morphology and porosity. It is important to be able to predict the droplet size distribution for a given geometry of an atomizer and its operation conditions. In rotary atomizers the liquid is first supplied to the internal atomizer reservoir, flows from there into several inserts (mainly driven by the centrifugal force associated with the atomizer rotation) and then it is ejected into the air. The jets of the ejected liquid then breakup and atomize into drops. Besides the spray drying industry [3, 4, 5] rotary atomizers [6, 7] and ligament based atomization is also used in numerous other applications, e.g. painting purposes [8]. The primary atomization process for laminar operating rotary atomizers has already been expressed in terms of non-dimensional numbers [9, 10], but such atomizers operate at much lower rotational speeds compared to the atomizers investigated in this study.

The most important parameter for the atomization process is the jet thickness at the exit of the inserts, because the initial jet thickness corresponds directly to the resulting droplet diameter D_{32} . Therefore in this study the jet thickness at the exit of the inserts is measured with a high-resolution imaging system and compared to numerical simulations. Furthermore, the drop size and velocity is measured with the time-shift (TS) technique [11] to gain a better understanding of the atomization process. Additionally, an analytical model is developed which is able to predict the rivulet flow in the insert of the rotary atomizer wheel and provide a basis on which the droplet size after the atomization can be estimated.

Material and methods

The experimental setup for the two different measurement campaigns conducted is shown in figure 1. The setup consists of the liquid supply system, an atomizer, alternatively, a high-resolution imaging system (figure 1(a)), or a laser based spray characterization system (figure 1(b)). The atomizer used in this investigation is fed by water, operated under normal ambient conditions and is provided by GEA Denmark [2]. A spray trap surrounds the atomizer wheel and catches the water exiting the inserts. The rotational speeds (10 500 1/min to 29 000 1/min) and feed rates (100 kg/h to 300 kg/h) are varied in the experiments. The mechanism of the primary atomization is observed using a high-resolution imaging system, consisting of a pco.edge 5.5 camera and a CAVILUX HF laser system (see figure 1(a)). The camera has a resolution of 2560 px × 2160 px and a Nikon AF Micro Nikkor lens with 105 mm focal length is used in the experiments. The CAVILUX HF laser is triggered by a tachometer signal of the atomizer and generates light pulses of 1 μ s duration at a frequency of 30 Hz. The camera is only capable of running at 50 Hz in global shutter mode, which is why the tachometer signal of the atomizer has to be skipped and only every 6-17 revolution can be captured, due to the high speed of the atomizer. The emitted laser light is deflected by

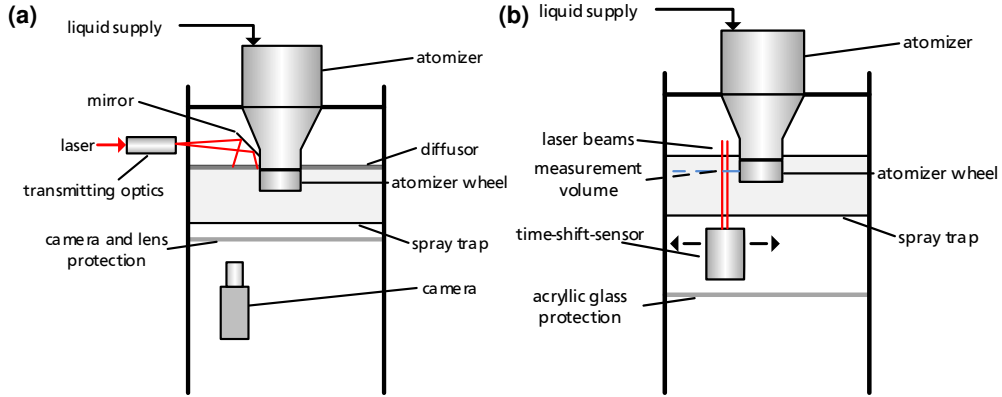


Figure 1. (a) Schematic experimental setup including: liquid supply system, atomizer and high-resolution imaging system. (b) Alternative experimental setup with the laser spray diagnostic system to measure droplet size and velocity. The TS sensor can be moved laterally to perform measurements at different positions.

a mirror, since, due to the design of the atomizer, a straight mounting of the laser is not possible. A diffusor plate is used to generate a more uniform background illumination in the photographs. Due to load fluctuations the speed of the wheel differs slightly over time, which leads to a small change in the field of view (FOV), and, therefore, a variation of the position of the insert. In the postprocessing this variation has to be corrected to be able to generate an average picture of the atomization process, which represents the thickness of the jet for one set point. The images (compare to figure 4) are rotated around the imaginary center point (which is outside the picture itself) and in the end cropped to the selected FOV.

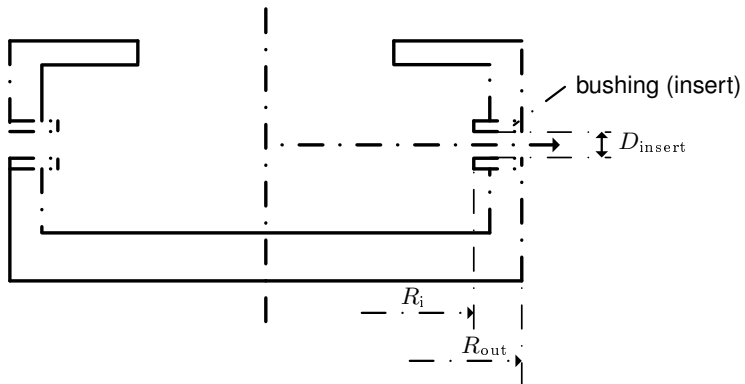


Figure 2. Sketch of the atomizer wheel in side view. $R_i = 35 \text{ mm}$, $R_{\text{out}} = 50 \text{ mm}$, $D_{\text{insert}} = 4 \text{ mm}$

The spray is then characterized using the time-shift technique: The diameter and the radial velocity are measured for each detected drop. The TS sensor is placed below and perpendicular to the atomizer wheel (see figure 1(b)), while the measurement position can be changed manually by moving the sensor laterally in a range of 30 mm to 70 mm distance to the rotary atomizer wheel. In figure 2 a sketch of the atomizer wheel side view with its geometric dimensions is shown.

Numerical simulations

Numerical simulations (CFD) are used to obtain a better understanding of the hydrodynamics inside the insert, as this area of the atomizer wheel cannot be accessed in the experiments. At the present stage of this study the CFD results are used as a qualitative visualization - but nevertheless, a short description of the simulations carried is given. The simulations are performed using ANSYS FLUENT. A Volume of Fluid (VOF) approach is used to represent the two phases. The face fluxes near the phase interface are calculated using the GEO-RECONSTRUCT scheme. Gravitation and surface tension force is included. Due to the periodic layout of the geometry, only one quarter of the wheel has been modelled. Periodic boundaries are applied at each side of the computational domain. The model is further simplified such that the inner part of the wheel is omitted, as it should not influence the flow in the outer part of the wheel. It is assumed that capturing the transport of water from the inside of the wheel to the inner periphery of the wheel is of no importance to the flow inside the bushings. The inner periphery of the wheel is given a zero gradient, zero flux boundary condition (symmetry boundary condition). The outlet of the model is given a zero gage

pressure outlet boundary condition. To model the transport of water from the inner part of the wheel to the water residing around the bushings, a source term for mass and momentum is applied to the cells in the water phase near the water/air interface. A conformal hexahedral mesh with 900 000 cells is used for the calculations. The mesh is stretched such that the bushing film flow is well resolved. The mesh inside the wheel is stretched such that the air/water interface is well resolved.

Time-Shift technique

One part of the experiments is carried out with the help of the TS technology to measure droplet size and velocity to gain a better understanding of the atomization process (compare to figure 1(a)). Therefore the TS technology is explained shortly, where more detailed descriptions are referenced. The TS technology was introduced by Semidetnov in 1985 [12] and developed further in work by Damaschke et al. (2002) [13] and Schäfer (2013) [11]. It is an optical technology which is based on the light scattering of a single particle from a shaped light beam. In figure 3 the basic measurement principle is explained on the basis of a spherical particle which is moving with velocity v_z through a laser beam with a Gaussian intensity profile.

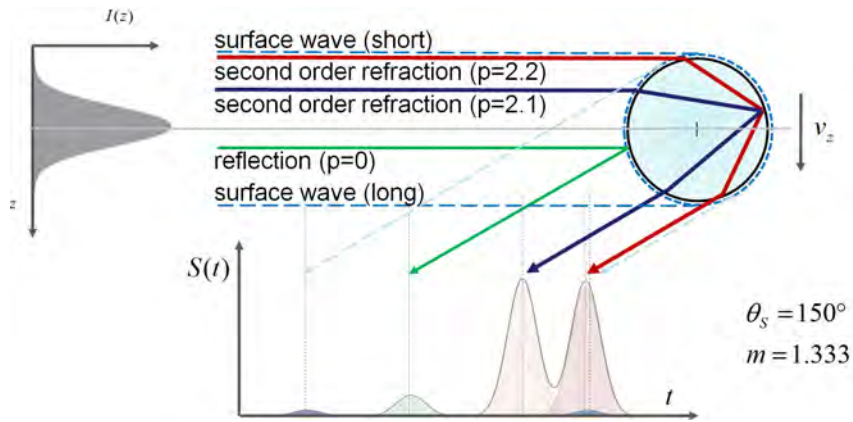


Figure 3. Basic principle of the time-shift technique. A Gaussian (left) beam is reflected on a moving, spherical and transparent particle (right) which leads in near backscatter (scattering angle Θ_s) to the time-shifted signals of four scattering orders: The short-path surface wave, the reflection, two modes of second-order refraction and the long-path surface wave. [11]

The detected signal from this near backscatter detection consists of the short-path surface wave, reflection, two modes of second-order refraction and the long-path surface wave. The scattered intensity peaks are detected at a single constant angle (Θ_s) for a specific refraction index of the particle (m). The spatial intensity profile of the light beam ($I(z)$) is transformed into a temporal signal of the detector ($S(t)$). The signal is the sum of all scattering orders like reflection ($p = 0$) and second-order refraction ($p = 2$) with their backscatter modes ($p = 2.1$ and $p = 2.2$) [11]. The mathematical description of the time dependent signal can be expressed in the general form:

$$I(z) = I_0 g(z, b) \xrightarrow{v_z = \frac{z}{t}} S(t) = \sum_p A_p g_p \left(v_z \left(t - t_0^{(p)} \right), b \right). \quad (1)$$

The width of the illumination with the maximum intensity I_0 is b . The intensity distribution is $g(z, b)$ and A_p are the sampling amplitudes of the scattering orders. v_z is the particle moving velocity in the scattering plane and normal to the illuminating beam and $t_0^{(p)}$ is the relative time position of the scattering order p or of a mode of a particular scattering order (number of internal refractions). A_p and $t_0^{(p)}$ depend on the scattering angle, the relative refractive index and the particle size. $S(t)$ is the time-shift signal, from which the particle size can be extracted if the velocity, the scattering angle and the relative refractive index are known [11].

$$\Delta s = \text{FWHM} \left\{ A_p g_p \left(v_z \left(t - t_0^{(p)} \right), b \right) \right\} = \frac{b}{v} \quad (2)$$

Equation (2) describes the correlation between the time width of the individual peaks in a TS signal at full width at half maximum (FWHM), the particle velocity v_z and the width of the illumination beam b . Knowing b and the width of the peaks Δs , the particle velocity can be easily calculated [11]. The particle diameter d can be calculated using the time separation between the peaks Δt :

$$\Delta t = \frac{d}{v} f(m, \Theta_s) = t_0^{(p=a)} - t_0^{(p=b)} \quad (3)$$

The function $f(m, \Theta_s)$ can be determined using geometric optics or Lorentz-Mie scattering codes. More details about signal validation and interpretation can be found in [11].

Results and discussion

Part I - Jet thickness

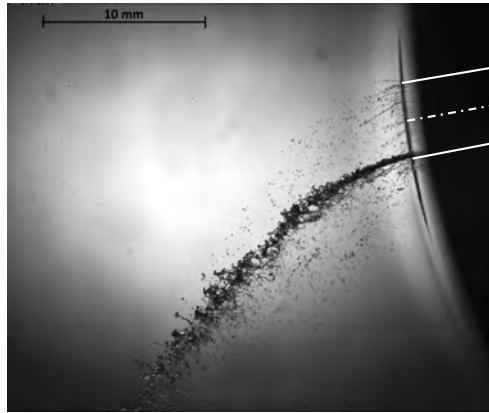


Figure 4. Photographic image of a jet (Speed: 10500 rpm, Feed rate: 100 kg/h). The opening of the insert is highlighted with white lines. The direction of the rotation is indicated by the arrow.

A typical photographic image recorded with the high-resolution imaging system visualizing the jet exiting the atomizer wheel is shown in figure 4. The opening of the insert is highlighted with white lines and the wheel is moving in the upwards direction (as indicated by the arrow). The liquid enters the insert inside the wheel and the whole periphery is wetted. The photographic images of the atomization (see figure 4) clearly show, that the main part of the liquid exiting the insert is concentrated at the trailing edge of the insert, whereas a small amount of liquid is visible around the entire periphery. This effect is caused by the Coriolis force, which acts azimuthal in the direction counter to the wheel rotation. A thin annular film still remains on the periphery of the insert, which becomes visible by the small droplets around the insert. The Coriolis force must exceed the surface tension, that tries to keep the liquid on the periphery of the insert. This effect can be seen on all conducted measurements for different set points.

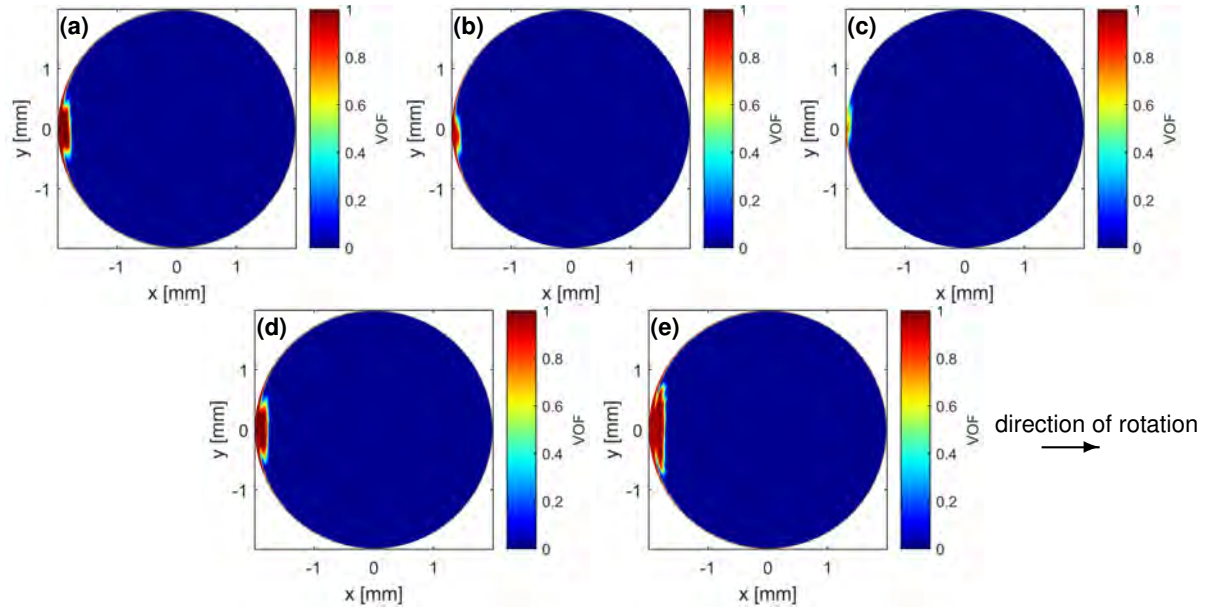


Figure 5. Results obtained with the help of CFD. The plots are coloured by the VOF and show the intersection of the inserts on the exit. Besides the jet on one side of the insert, an annular film flow can be seen around the periphery of the insert. (a) Case 1: 10 500 1/min, 100 kg/h (b) Case 2: 20 000 1/min, 100 kg/h (c) Case 3: 29 000 1/min, 100 kg/h (d) Case 4: 20 000 1/min, 200 kg/h (e) Case 5: 20 000 1/min, 300 kg/h (see table 1 for comparison)

The results from the numerical simulations are very helpful to obtain a better understanding of the flow inside

the insert. In figure 5 the VOF distribution from the CFD simulations on the exit plane of the insert is plotted for different set points. Similar to the photographic image, the liquid accumulates on the trailing edge (direction of movement is from left to right) of the insert and the thickness of this jet varies with different operating parameters. Besides the position of the jet, a thin annular film can be seen on all pictures. This annular film wets the whole periphery and matches with the experimentally obtained photographic images. In contrast to the experimentally obtained results, the CFD results can be used as an estimation of the mass flow distribution in the annular film and the jet. Although the annular film is very thin (on the leading edge $h \approx 20 \mu\text{m}$), the mass flow rate of the film $\dot{Q}_{film} = \dot{Q} - \dot{Q}_{red}$ (compare to table 1) is between 25 % to 55 % of the total mass flow rate \dot{Q} . The experimentally obtained photographic images don't indicate the importance of the thin annular film flow in the insert (compare to figure 4). Around the periphery only small droplets are visible, that seem to be negligible in comparison to the jet.

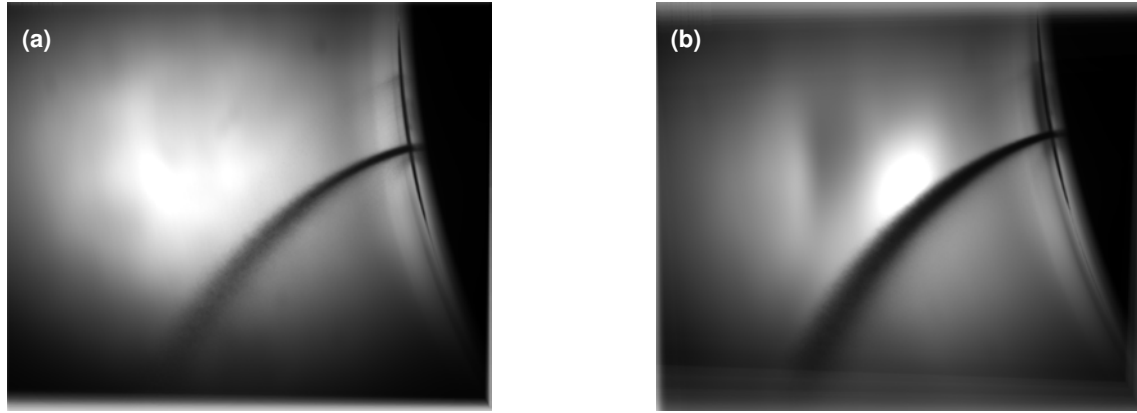


Figure 6. Mean photographic images of the atomization process for two different set points. Individual images have been rotated around the imaginary center point of the atomizer wheel to compensate for load and therefore FOV fluctuations. (a) Speed: 10 500 1/min, Feed rate: 100 kg/h (b) Speed: 20 000 1/min, Feed rate: 200 kg/h

To be able to compare the thickness of the jets exiting the inserts from the experiments and the numerical simulations, the jet thickness has to be measured from the photographic images. The resolution of the images is $11.76 \mu\text{m}/\text{px}$. As the single pictures show slight load fluctuations, the thickness of the jet varies over time. To compensate this behaviour mean images are generated (as shown in figure 6) and used to measure the jet thickness. Across the insert the grayscale or intensity values are plotted (compare figure 7) and the jet thickness can be estimated depending on the threshold value that is used. The speed of the wheel and the mass flow rate are varied to get a good estimation of the behaviour of the jet thickness for variable operating parameters. The results for the thickness estimation of the jet from the experimentally obtained photographic mean images for different set points is shown in Table 1 ($h_{jet,EFD}$). Additionally a theoretical model is developed to describe and predict the flow in the insert. An approximate solution of the flow in the rivulet inside the insert is obtained from the mass and momentum balance equations. A kinetically admissible flow in the rivulet cross-section is assumed which satisfies the no-slip conditions at the wall. Then the momentum balance equation is formulated which accounts for the inertial effects, associated with the rotation of the atomizer (Coriolis force), inertia of the liquid in the rivulet, and viscous stresses. The evolution equation for the rivulet depth h is obtained in the form

$$-\frac{3969\rho Q^2 h'(Z)}{2288\sqrt{2}\sqrt{R_{insert}}h(Z)^{5/2}} + \frac{63\mu Q}{16h(Z)^2} - \frac{1}{3}4\sqrt{2}\rho\sqrt{R_{insert}}\omega^2 Z h(Z)^{3/2} = 0 \quad (4)$$

with the liquid density ρ , the mass flow rate per insert Q , the film thickness h , the radius of the insert R_{insert} , the

Table 1. CFD mass flow rates \dot{Q} and resulting jet thickness h_{jet} for different cases. The reduced mass flow rate \dot{Q}_{red} only considers the jet, whereas \dot{Q} represents the total water mass flow rate (annular film flow and jet). The mass flow rates are obtained from the CFD results. CFD: numerical simulations, EFD: experiments, AFD: analytical model

	RPM [1/min]	\dot{Q} [kg/h]	\dot{Q}_{red} [kg/h]	$h_{jet,CFD}$ [μm]	$h_{jet,EFD}$ [μm]	$h_{jet,AFD}$ [μm]
Case 1	10500	98.40	70.80	176	300	191
Case 2	20000	99.04	60.84	140	260	125
Case 3	29000	95.64	42.68	80	235	98
Case 4	20000	195.44	146.00	192	430	196
Case 5	20000	297.64	222.44	273	525	256

dynamic viscosity μ and the angular velocity ω , in dependency of the axial coordinate in the insert Z . Differential equation (4) can be solved numerically subject to initial conditions for the rivulet depth at the entrance $Z = R_i$. At this point the thickness is comparable with the insert radius R . It was shown that the jet thickness at the exit from the insert only slightly depends on the initial conditions. In the further analysis all the jet thicknesses are computed using the initial conditions $h = R_{\text{insert}}/2$ at $Z = R_i$. Theoretical predictions for the jet thickness h at the exit from the insert ($Z = 50$ mm) are shown in Table 1 together with the numerical and experimental results.

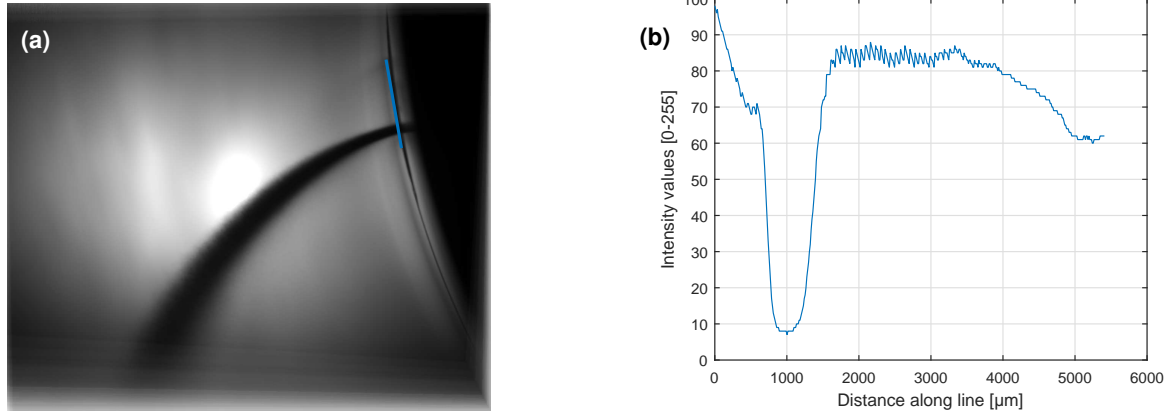


Figure 7. (a) Mean photographic image and the highlighted line at which the intensity values are evaluated to get the jet thickness. (Speed: 20 000 1/min, Feed rate: 300 kg/h) (b) Plot of the intensity (grayscale) values along the line shown in the left picture. The jet is clearly distinguishable from the background, which makes it possible to measure the jet thickness (depending on the threshold value that is used).

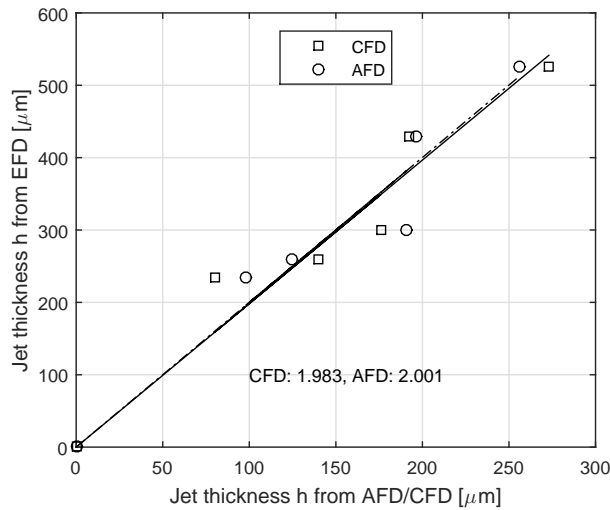


Figure 8. Comparison of experimentally obtained rivulet thickness with CFD results and analytical estimation (see equation (4)). The numbers in the graph show the slope of the curves.

Figure 8 shows the comparison of the jet thickness predicted from CFD, theoretical predictions from the solution of Eq. (4) (AFD) with the experimental data (EFD). The observed jet thickness changes linearly with the predicted values. This indicates that the main phenomena in the computations and in the theoretical predictions are identified and described correctly. The measured thickness of the jet is however nearly twice of the predicted data. This is explained by the waves on the rivulet interfaces, which are not accounted for in the models. The interfacial instabilities result in a variation of the jet thickness at the exit. The averaging of the jet thickness over many instants leads to a systematic increase of the size of the jet. Besides that, the experimentally obtained jet thickness is not a fixed value, as a variation in the greyscale threshold leads to a variation of the jet thickness. Also the load fluctuations (leading to a rotational error of the FOV) and the adjustment in the postprocessing of the data is, at the current stage of the study, not flawless. The adjustment of the rotation due to load fluctuations works with a resolution of $\Delta\alpha = 0.05^\circ$, which causes a possible error of $\Delta h = 44 \mu\text{m}$. Another issue is the illumination time of the laser for the photographic images of $\Delta t = 1 \mu\text{s}$, causing a motion blur depending on the rotational speed of the

wheel. The upper limit of the error caused by the motion blur can be estimated by $\Delta h = \omega R_{\text{out}} \Delta t$ to $\Delta h \approx 55 \mu\text{m}$ for 10 500 1/min and $\Delta h \approx 152 \mu\text{m}$ for 29 000 1/min. To eliminate this motion blur future investigations will be conducted with a high power short-pulse laser ($\Delta t = 10 \text{ ns}$).

Part II - TS measurements

As shown in figure 9(a), the droplet Sauter mean diameter D_{32} decreases with increasing rotational speed of the atomizer, as expected. The feed rate only has a minor influence on the resulting D_{32} , whereas the influence increases with increasing speed. In the experiments a higher feed rate causes a higher data rate, resulting in more detected droplets per time and only a minor change in the diameter. Besides the droplet diameter the TS technique can also measure the velocity of the detected droplets in radial direction (depending on the alignment of the sensor), as shown in figure 9(b). With increasing speed of the wheel the radial velocity \bar{u}_r of the droplets increases and varies slightly with the mass flow rate. The velocity trend clearly shows a limiting value around $\bar{u}_r = 40 \text{ m/s}$, possibly due to an increase of drag for higher velocities, as the droplet velocity is measured 50 mm in front of the insert exit.

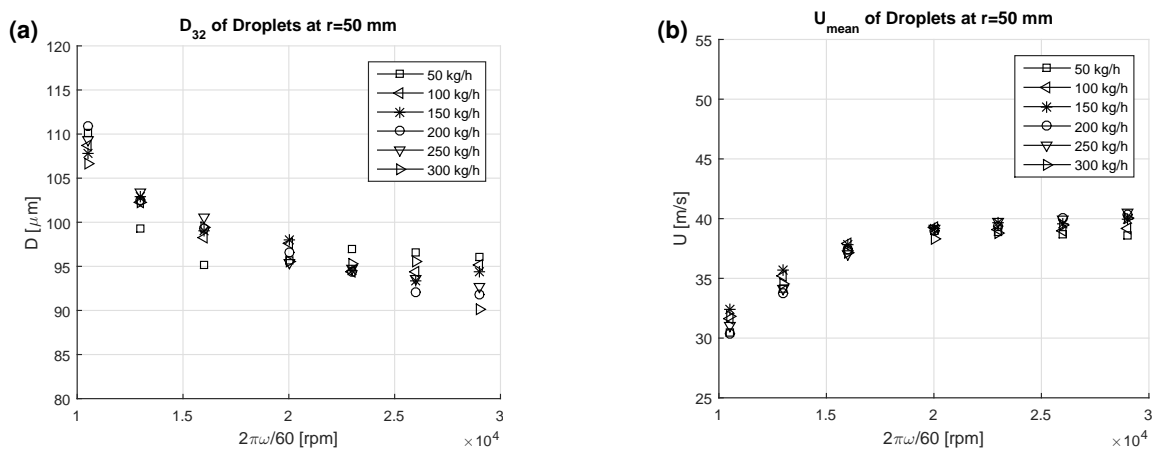


Figure 9. (a) Sauter mean diameter D_{32} obtained from experiments as a function of rotational speed and feed rate. (b) Mean radial droplet velocity \bar{u}_r obtained from the TS measurements.

Linking both experiments (Part I and Part II) it becomes clear that the droplet size depends on the thickness of the rivulet exiting the insert of the atomizer (see figure 10). As the film thickness h and therefore the droplet diameter D_{32} depend on ω^2 , the speed of the wheel has the largest influence on the outcome of the atomization process. The influence of the feed rate is rather weak compared to the influence of the rotational speed, as the range is limited to a much smaller scale.

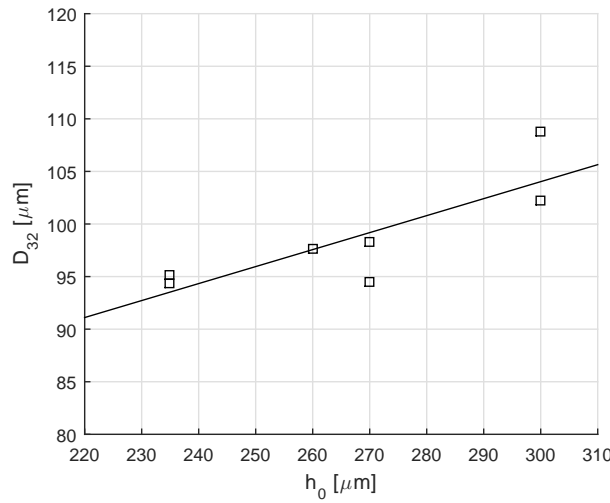


Figure 10. Experimentally (TS) obtained D_{32} compared to the initial jet thickness $h_{\text{jet},\text{EFD}}$.

Conclusions

In this experimental, computational and theoretical study the atomization of a Newtonian liquid in a rotary atomizer is investigated in detail. The numerical study shows that the liquid in the insert flows mainly in a rivulet. The depth of the rivulet is determined by the geometry of the atomizer and the rotational velocity, as well as by the liquid properties and volumetric flux. A theoretical model is developed, that is able to predict the evolution of the rivulet depth in the insert. The predicted values of the jet thickness at the insert exit behave nearly linearly with the observed rivulet thicknesses. The spray generated by the atomizer has been characterized using the time-shift technique. It is shown that the measured data for the average drop diameter correlates well with the jet thickness. Therefore, the diameter of the drops in the spray generated by rotary atomizer can be predicted using theoretical or computational models of the rivulet flow.

Nomenclature

h	film thickness [m]	ρ	density [kg/m^3]	R_{out}	radial pos. end insert [m]
C	correction factor [-]	R_{insert}	insert radius [m]	R_i	radial pos. beg. insert [m]
μ	dynamic viscosity [Pa s]	Z	axial insert pos. [m]	D_{insert}	insert diameter [m]
Q	feed rate [m^3/s]	ω	angular velocity [rad/s]	Θ_s	scattering angle [$^\circ$]
m	refractive index [-]	I	intensity profile [-]	D_{32}	sauter mean diameter [m]
\bar{u}_r	mean radial velocity [m/s]				

References

- [1] GEA Process Engineering A/S. http://www.gea.com/global/en/binaries/GEA%20Spray%20drying%20absorption%20Waste%20Incinerator_tcm11-24419.pdf ([online]. [cit. 2016-01-29]).
- [2] GEA Process Engineering A/S. <http://www.gea.com> ([online]. [cit. 2016-01-29]).
- [3] Mujumdar, A. S., 2014. "Handbook of Industrial Drying". CRC Press, Boca Raton.
- [4] Baker, C., 1997. "Industrial Drying of Foods". Springer Science & Business Media, Heidelberg.
- [5] Masters, K., 1979. "Spray Drying Handbook". G. Godwin ; Halsted Press, London; New York, 3. ed.
- [6] Ashgriz, N., 2011. "Handbook of Atomization and Sprays: Theory and Applications". Springer US, New York.
- [7] Liu, H., 2000. "Science and Engineering of Droplets: Fundamentals and Applications". Noyes Publications Andrew, Park Ridge, NJ Norwich, NY.
- [8] Domnick, J. Sep. 2.-6. 2012, 12th Triennial International Conference on Liquid Atomization and Spray Systems, Heidelberg, Germany.
- [9] Walzel, P., Schaldach, G., and Wiggers, H. Sep. 8.-10. 2008, 22nd European Conference on Liquid Atomization and Spray Systems, Como Lake, Italy.
- [10] Mescher, A. and Walzel, P. Sep. 6.-8. 2010, 23rd Annual Conference on Liquid Atomization and Spray Systems, Brno, Czech Republic.
- [11] Schäfer, W. and Tropea, C., 2014. *Applied Optics*, 53(4), pp. 588–597.
- [12] Semidetnov, N., 1985. "Investigation of laser Doppler anemometer as instrumentation for two phase flow measurements". Ph. D. thesis, Leningrad Inst. Precis. Mech. Optics.
- [13] Damaschke, N., Nobach, H., Semidetnov, N., and Tropea, C., 2002. *Applied Optics*, 41(27), pp. 5713–5727.